Effect of TiC incorporation on the optical properties and oxidation resistance of SiC ceramics

Héléne Arena, Moustapha Coulibaly, Audrey Soum-Glaude, Alban Jonchere, Guilhem Arrachart, Adel Mesbah, Nicolas Pradeilles, Marion Vandenhende, Alexandre Maître, Xavier Deschanels

Effect of TiC incorporation on the optical properties and the oxidation resistance of SiC ceramics

Hélène Aréna[1*], Moustapha Coulibaly[1], Audrey Soum-Glaude[2], Alban Jonchère[1], Guilhem Arrachart[1], Adel Mesbah[1], Nicolas Pradeilles[3], Marion Vandenhende[3], Alexandre Maître[3], and Xavier Deschanels[1]

[1] ICSM, CEA, CNRS, ENSCM, Univ. Montpellier, Marcoule, 30207 Bagnols-sur-Cèze, France
[2] PROMES-CNRS, UPR 8521, 7 rue du Four Solaire 66120 Font-Romeu Odeillo Via, France
[3] IRCER, UMR CNRS 7315, 87068 Limoges, France

Corresponding authors: helene.arena@cea.fr and xavier.deschanels@cea.fr

Keywords: SiC, TiC, nano composite, oxidation resistance, optical properties, CSP, high temperature, ceramics, reflectance.

Abstract

In concentrating solar power (CSP) technologies, the absorber material should be spectrally selective under severe operating conditions, i.e. ~1000°C under air atmosphere. SiC-TiC nanocomposites could be good candidates for this application due to their spectral selectivity at room temperature, but their behavior under CSP operating conditions is unknown. Therefore, the spectral selectivity and oxidation resistance of TiC-SiC composites were studied up to 500 °C, under air, for various compositions. During heating, the emittance increased with the temperature. After heating, the TiC grains at the surface were oxidized into TiO_2, while SiC grains showed good behavior. However, despite little oxidation, the spectral selectivity of the nanocomposites remained interesting after heating. Specific oxidation tests up to 9 days at 1000°C under air showed an increase of the oxidation resistance with the amount of SiC. This result is the consequence of the formation of a protective layer of SiO_2 preventing the oxidation of the TiC grains. The composition 30 at% TiC – 70 at% SiC seems to be a good compromise between low oxidation and good selectivity.

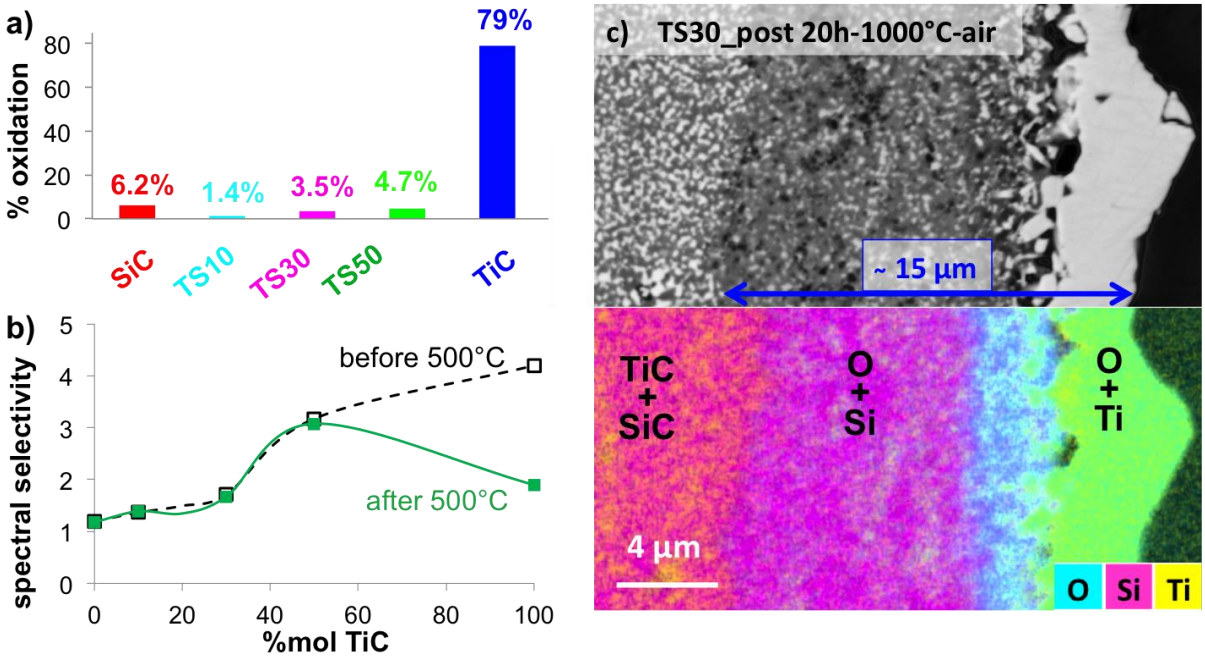

1. Introduction

Solar energy is a powerful source of renewable energy which can be efficiently exploited by Concentrating solar power technologies (CSP) [1, 2]. In this promising and sustainable systems, the sunlight is collected by several heliostats and concentrated towards the absorber. The absorber converts the solar radiation into heat and transfers it to a thermal fluid, which will drive a turbine in power block to generate electricity. However, when heated by sunlight, the absorber may behave as a blackbody and lose some energy by thermal emission. To maximize its efficiency, the ideal absorber should be spectrally selective, i.e., have a high absorptance in the sunlight region (0.25-2.5 µm) and a low infrared emittance in the blackbody region (typically 1.25-25 µm at 500 °C) [3-6]. The Carnot efficiency of the solar thermal power plants increases when increasing the working temperature [7, 8]. Therefore, the absorber must also be able to maintain good mechanical, physical and chemical properties under severe operating conditions (T ~ 1000 °C under air atmosphere).

Silicon carbide (SiC) is the material commonly used as the absorber because of its high resistance to oxidation and its good sunlight absorptance. The surface oxidation of SiC leads to the formation of an amorphous SiO_2 passivating layer. This SiO_2 layer protects the SiC underneath up to temperatures of 1400 °C [7]. However, SiC has a high thermal emittance leading to significant energy losses in the infrared region, especially when increasing the working temperatures [9, 10].

Thanks to their spectral selectivity, metal borides, nitrides or carbides could be good candidates for solar absorber applications [11-24]. In addition, these materials have extremely high thermal stability, good thermo-chemical and thermo-mechanical properties, high hardness, high electrical and thermal conductivities [25-28]. Coulibaly *et al.* compared the optical properties of several carbides and demonstrated that titanium carbide (TiC) is one of the best compound in this group, due to its particularly low emittance [29]. However, the major limitation of this material is its low resistance to oxidation [30-37].

To improve both the optical selectivity of SiC and the oxidation resistance of TiC, they can be combined in a nanocomposite structure [29, 38]. Indeed, the association of SiC and TiC showed better optical selectivity than pure SiC and better oxidation resistance than pure TiC. According to Banu *et al.*, the oxidation of a TiC/SiC composite material produced TiO_2/SiC up to 750 °C, and a TiO_2/SiO_2/SiC mixture at higher temperatures [39]. The addition of SiC increased the oxidation resistance of ZrC [40], ZrB_2 and HfB_2 materials [26, 41].

In a previous paper [38], we have shown how the porous characteristics (density and surface roughness) can change the selectivity of SiC 70% at. –TiC 30% at. nanocomposite at room temperature. In this paper, we studied the mutual dependency between the TiC content, the oxidation resistance and the spectral selectivity by reflectance measurements at various temperatures up to 500 °C, and thorough material characterization. To go further on the assessment of the oxidation resistance, the samples were also heated to 1000 °C under air during 20 h to 9 days to precise the nature of the oxide layers.

2. Experimental

The complete synthesis route, starting materials, sample preparation and characterization techniques used are described in detail in Supplementary Information (SI 1) and in our previous paper [38]. The main information are given below.

A “molecular route” involving hydrolysis and polycondensation of alkoxides as metal oxide precursors, and sucrose and citric acid as carbon sources was used to synthesize the nanocomposites [42]. Two heat treatments were used to transform the resulting oxide powders into carbides; the decomposition of the organic part into carbon (800 °C – 4h – under Ar), and then, the carbothermal reduction (1550 °C – 4h – under Ar). Composites with increasing Ti/Si proportions were produced by this molecular synthesis route and commercial powders were used for the pure TiC and SiC reference samples (Table 1). Dense materials were produced by

Spark Plasma Sintering (Syntex, Dr. Sinter 825, Japan), with sintering temperatures of 1700°C for TiC, 1950°C for SiC and 1750°C for the composites. The densified materials were mirror polished (Beta Buehler grinder-polisher), using SiC grinding papers and 1 µm diamond paste (Struers). The samples density and porosity was evaluated using Archimedes method, helium pycnometry and the proportions of Ti, Si, O and C determined by elemental analysis (C and O wt% - LECO CS230 and TCH600), and X-Ray Fluorescence (Spectro-Xepos).

Sample name	**TS10**	**TS30**	**TS50**	**TiC**	**SiC**
Origin	Sol-gel synthesis route			Commercial products	
Ti / Si (%at)	10 / 90	30 / 70	50 / 50	100 / 0	0 / 100
Ti / Si (%wt)	14.3 / 85.7	39 / 61	60 / 40	100 / 0	0 / 100
Tsintering (°C)	1750			1700	1950

Table 1: Name, composition and sintering temperature for all samples. "TS" refers to TiC-SiC composite materials, the number across refers to the at% of TiC. For example, TS10 = 10 %at TiC – 90 %at SiC.

All samples were characterized in terms of: (i) roughness by optical interferometry (Fogale Nanotech), (ii) morphology and composition by Scanning Electron Microscopy (SEM - FEI Quanta 200 ESEM) coupled with Energy Dispersive X-ray Spectrometry (EDX - Bruker SDD 5030 detector), (iii) structure by X-Ray Diffraction (XRD) and Grazing Incident X-Ray Diffraction (GI-XRD) with an incident angle of 0.4° (Bruker D8_10-90° (2θ)), and (iv) optical properties through the measurement of the reflectance in the 0.25 to 25 µm range of wavelengths (Perkin Elmer Lambda 950 with a 150 mm integrating sphere coated with Spectralon, and a SOC-100 HDR coated with gold and using a 700 °C (973 K) blackbody). A heating plate on the sample holder enabled measurements at different temperatures (from room temperature to 500 °C). The temperature of the sample was controlled by a surface thermocouple connected to PID (proportional–integral–derivative) regulation of the heating resistance. The complete description of the devices used for reflectance measurements is detailed in [43, 44]. The absorptance (α), *i. e.* the propensity of the material to absorb sunlight, was calculated in the range of wavelengths (λ) 0.25 to 4 µm, from the total spectral reflectance $R(\lambda,T_a)$ measured at room temperature (T_a), and the standard solar irradiance spectrum $G(\lambda)$, according to Equation 1. The directional emittance ($\varepsilon_{8°}$), *i. e.* the tendency of the material to emit thermal radiations, was calculated in the range of wavelengths 1.25 to 25 µm, from the total spectral reflectance $R(\lambda,T_a,8°)$ measured at various temperatures (T), and the spectral exitance of a blackbody $P(\lambda,T)$ at the same temperatures, derived from Planck's law (Equation

2). Since all samples were completely opaque, the transmittance was not calculated and considered null. The total spectral reflectance was measured at various detection angles (θ from 8 to 80°) to calculate the hemispherical emittance (ε_H) at room temperature (Equation 3).

$$\alpha = \frac{\int_{0.25\ \mu m}^{4\ \mu m}[1-R_{8°}(\lambda,T_a)]\cdot G(\lambda)\cdot d\lambda}{\int_{0.25\ \mu m}^{4\ \mu m} G(\lambda)\cdot d\lambda} \quad (1) \qquad \varepsilon_\theta(\theta,T) = \frac{\int_{1.25\ \mu m}^{25\ \mu m}[1-R(\lambda,T,\theta)]\cdot P(\lambda,T)\cdot d\lambda}{\int_{1.25\ \mu m}^{25\ \mu m} P(\lambda,T)\cdot d\lambda} \quad (2)$$

$$\varepsilon_H(T_a) = 2\int_0^{\pi/2} \varepsilon_\theta(\theta,T_a)\cdot\sin\theta\cdot\cos\theta\cdot d\theta \quad (3)$$

To measure the near-normal spectral reflectance at various temperatures, the samples were heated up to 500 °C (450 °C for TS30) as described in Figure 1 [44]. The atmosphere was not controlled during heating therefore the samples were submitted to oxidation. The samples were thoroughly characterized at room temperature before and after heating, using various techniques (SEM, (GI)XRD, and interferometry) to evaluate the effects of heating.

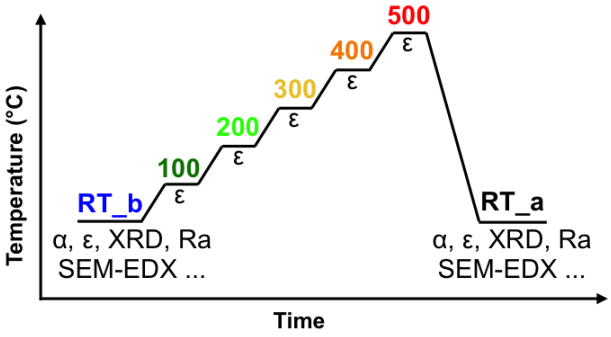

Figure 1: Heating procedure to measure the near-normal spectral reflectance at various temperatures. In the case of TS30, the maximum temperature was 450 °C.

Finally, thermogravimetric analyses (TGA) were conducted (Setsys 1750Cs Evol Staram). The oxidation resistance of all samples was evaluated when exposed to 20 h dwell at 1000 °C under air (10 °C.min^{-1} rise and 30 ° C.min^{-1} decrease).

3. Results

3.1. Materials characterization before heating

Physical shape

The composition and the characterisitics of the sintered materials are reported in Table 2. All samples except pure SiC had a relative density higher than 90 % and a surface roughness lower

than or equal to 10 nm. Pure SiC sample presented a lower relative density (74 %) due to is high covalency of the Si-C bonds which induces low self-diffusion coefficient [45, 46]. The SiC sample presented 26 % of open porosity which resulted in surface holes partly accounted when measuring the surface roughness (24 nm). On the contrary, TiC sample was more easily densified due to the presence of Ti-Ti metallic bonds in the structure. The association of TiC with SiC in a composite made the sintering easier compared to pure SiC and lead to denser and denser materials as the proportion of TiC increased.

According to SEM-EDX and XRF analyses, the composites had the expected Ti/Si propotions, also a little enrichement in Ti was observed for TS10 and TS50 samples. The O content was high in sample TS30 (5.5 wt%), even though the C content was equal to the amount required for stoichiometric SiC-TiC materials. This result suggests an incomplete carbothermal reduction, possibly due to a lack of homogeneization during the synthesis.

Sample	**Processing parameters**	**Composition**						**Sintered materials characteristics**			
	T sintering (°C)	**Ti / Si (at%)**				C (wt%)	O (wt%)	**Relative density (%)**	**Open porosity (%)**	**Closed porosity (%)**	**Surface roughness (nm)**
		Theory	XRF	SEM-EDX	**Average**						
TS10	1750	10 / 90	12 / 88	14 / 86	**13 / 87**	29.78	0.79	92.8	4.2	3	**4**
TS30		30 / 70	35 / 65	28 / 72	**32 / 68**	25.99	5.5	95.8	1.2	3.1	**10**
TS50		50 / 50	55 / 45	53 / 47	**54 / 46**	22.6	1.89	99.7	0	0.3	**3**
TiC	1700	100 / 0				19.6	0.46	96	1.2	2.8	**9**
SiC	1950	0 / 100				30.38	0.2	73.9	26.1	0	**24**

Table 2: Characteristics of all samples after sintering. The theoretical wt% of C is 30 %, 29 %, 26 %, 24 % and 20 % for pure SiC, TS10, TS30, TS50 and pure TiC, respectively. The standard errors are evaluated at 1 at% for Ti/Si proportion, 1 nm for surface roughness and 0.1 % for elemental analyses, relative density, and open and closed porosity.

Morphology and structure

Scanning Electron Microscopy was used to characterize the composition and the morphology of the sintered materials (Figure 2). In back-scattering electron mode, the TiC grains appear white, while the SiC matrix is gray. The size of the TiC grains is similar in all composite samples (about 150 nm) and their repartition is homogenous at a short range. Nevertheless,

when the TiC proportion increases (TS10 to TS30), the space between two TiC grains decreases and large TiC enriched domains are observed. In the TS50 sample, the TiC and SiC contents form two distinct domains with adjacent grains gathered in aggregates. In addition, all composites present large areas with variations in electronic contrast, which could be explained by local changes in porosity or composition. Here again, a better homogeneization of the precursors during the synthesis could improve the Ti – Si repartition; ongoing work is in progress to improve the mixing. In the case of the pure TiC sample, the grains are very small (< 100 nm) without any apparent porosity, while the pure SiC sample presents much bigger grains (about 5 μm) and the open porosity is evidenced by the presence of holes. The bigger grain size for pure SiC could be due to its higher sintering temperature (1950 °C vs 1750 °C for composites) and/or to the starting powders. Indeed, the composites were synthesized by the molecular route while the pure TiC and SiC originated from commercial powders.

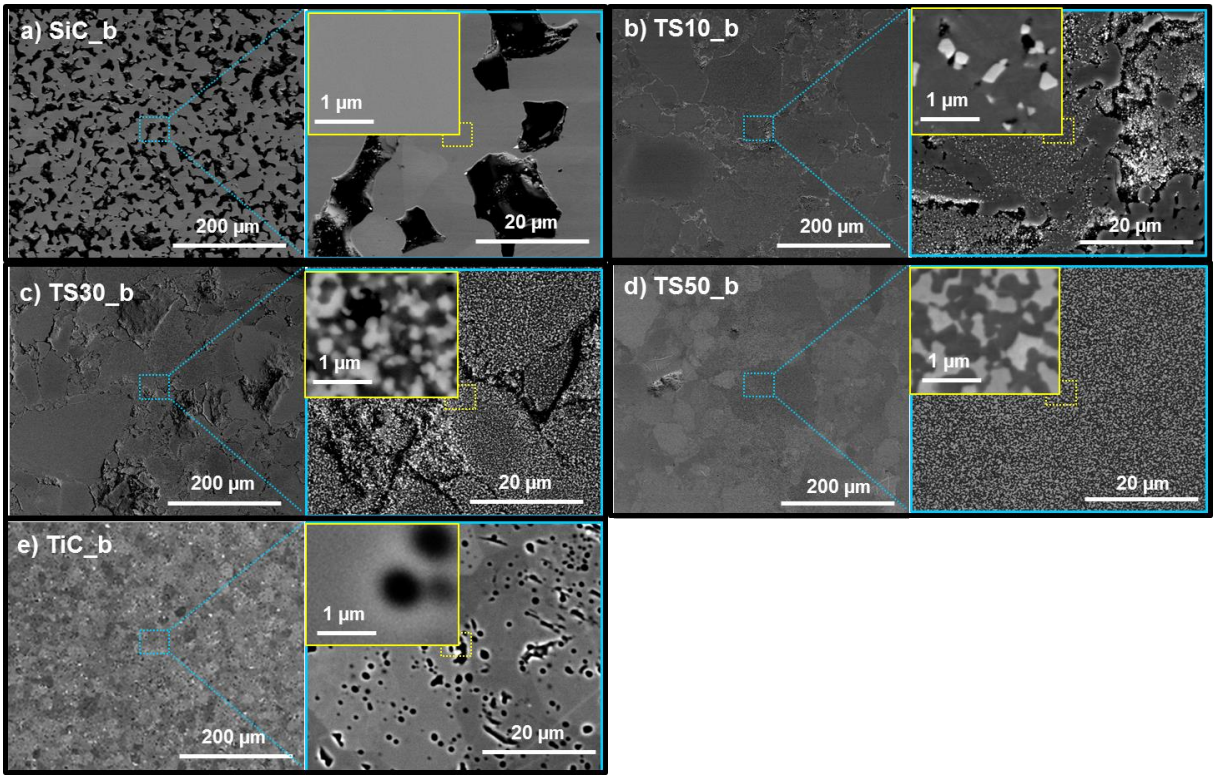

Figure 2: SEM images of the surface of the samples a) pure SiC, b) TS10, c) TS30, d) TS50, e) pure TiC. The "_b" stands for "before heating". Based on SEM images, the grain size was measured on several grains and locations, and a statistical average was considered.

The structure of the sintered materials was analyzed by XRD and the cubic 3C SiC (F-43m space group) and cubic TiC (Fm-3m space group) phases are identified (Figure 5 and SI 2). As expected, when increasing the TiC content, the relative intensities of the SiC peaks decreases, while those of the TiC peaks increases.

Optical properties

The optical properties of the samples were evaluated by the measurement of the total (specular + diffuse) spectral reflectance in the 0.25 to 25 μm wavelength range. At room temperature (Figure 3 blue curves, and SI 3), the reflectance of the SiC sample is much lower than that of TiC with a typical reflectance peak (~60 %) around 12 μm. The reflectance curves of the TiC-SiC composites are shaped like that of the SiC sample, with an increasing reflectance as the amount of TiC increases (SI 3).

3.2. Materials characterization during and after heating

Afterward, all samples were heated up to 500°C, to measure their total near normal spectral reflectance (heating procedure described in Figure 1). The reflectance curves obtained at several heating temperatures are reported in Figure 3, where (RT_b) and (RT_a) represent the room temperature measurements recorded before, and after heating, respectively. For all samples, and in the entire range of wavelengths, the reflectance decreases when increasing the temperature. In the case of pure SiC, the reflectance curves before and after heating are almost superimposable. On the contrary, for the TiC sample, the reflectance curve at 400 °C presents a strong decrease in the wavelengths range below 10 μm. At 500 °C, this decrease in reflectance goes on to the full range of wavelengths, and the reflectance curve presents oscillations. The reflectance measured at room temperature after heating (RT_a) is very different from the one measured before heating (RT_b), it is rather close to the one obtained at 500 °C, with even stronger oscillations. In the case of TS10 and TS30 composites, heating induces a decrease in reflectance but the shape of the curve is conserved. For the TS50 sample, the reflectance strongly decreases, particularly in the 0.25 to 10 μm range of wavelengths.

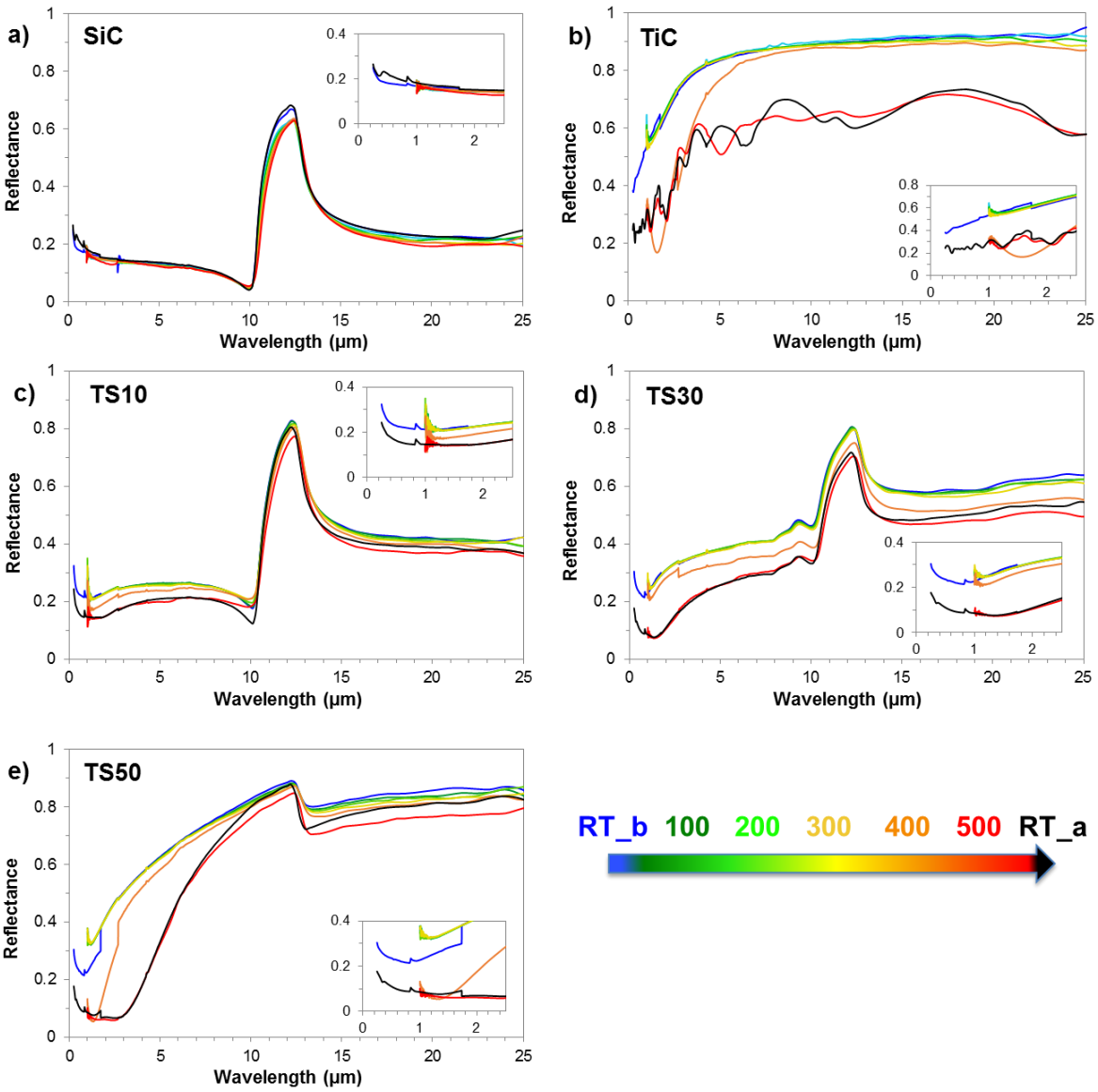

Figure 3: Near normal spectral reflectance at various temperatures (°C) for a) pure SiC, b) pure TiC, c) TS10, d) TS30 and e) TS50.

Surface characterization after heating provided explanations for these evolutions. For all samples, the surface roughness has increased (from 4 to 38 for TS10, 10 to more than 550 nm for TS30, 3 to 47 nm for TS50, 24 to 40 nm for SiC and 8 to 47 nm for TiC), which is confirmed by SEM observations (Figure 4).

The surface of the pure SiC sample appears to be intact, while the presence of titanium oxides is detected on the surface of all other samples. During their oxidation TiC grains expand by volume gain and they emerge from the initially polished surface (Figure 4-a). To study the thickness of the oxidized layer, sample pieces were embedded in a resin and polished (Figure 4-b). In the case of pure TiC sample, the surface is covered by a 2.3 µm thick crust of titanium

oxides with various morphologies. Underneath this zone, pristine TiC can be observed. In the case of the composites TS50 and TS30, the cross-section observations show no demarcation, indicating the presence of a significant layer of oxides on the surface of the sample. Only the TiC grains of the surface are oxidized, the SiC matrix seems to be intact.

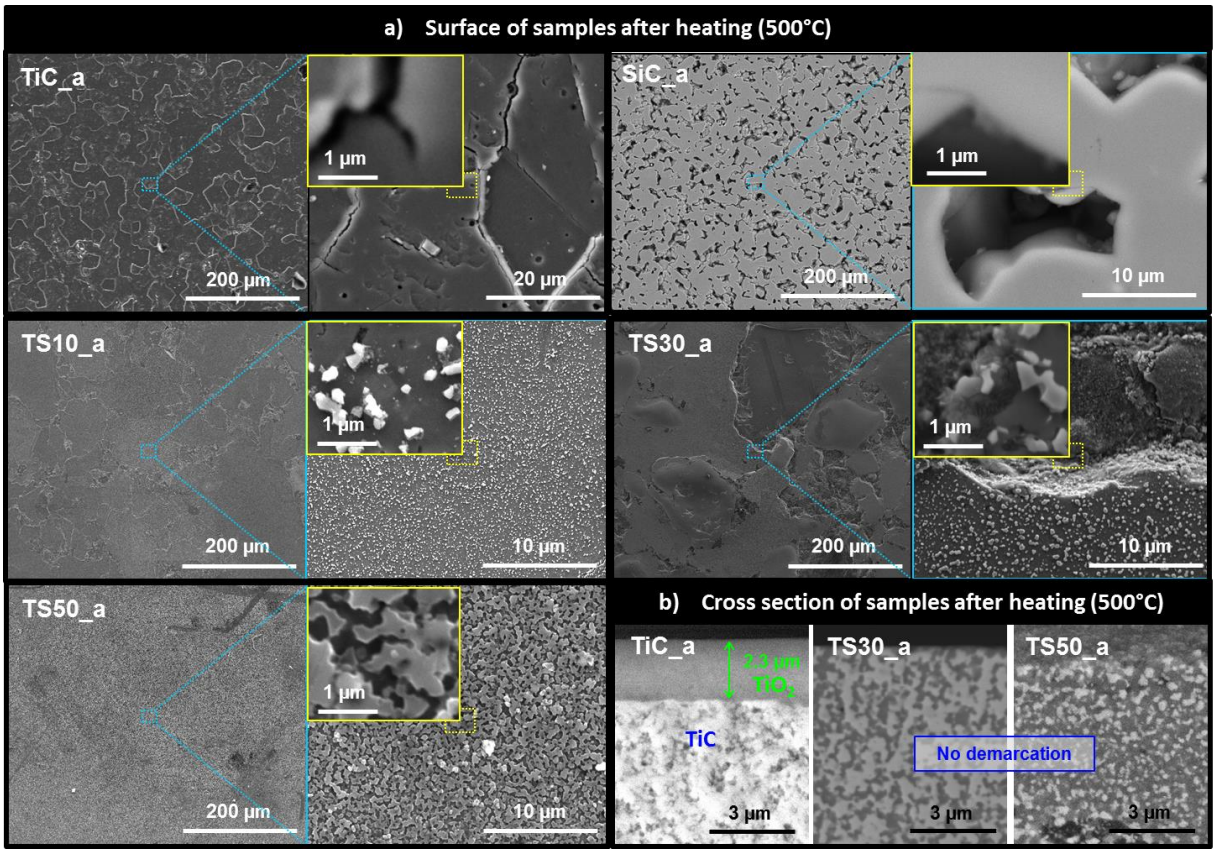

Figure 4: SEM observations after heating of a) surface of all samples and b) TiC, TS30 and TS50 in cross sections. The "_a" stands for "after heating".

The oxidation of TiC is also evidenced by the presence of the characterisic peaks of TiO_2 in all samples (GIXRD and XRD, Figure 6). At the extreme surface of the pure TiC sample, the signature of TiO phase could be seen as well. In most cases, the SiO_2 peaks are absent, suggesting that SiC has not been oxidized, or that the resulting phase is not cristallized.

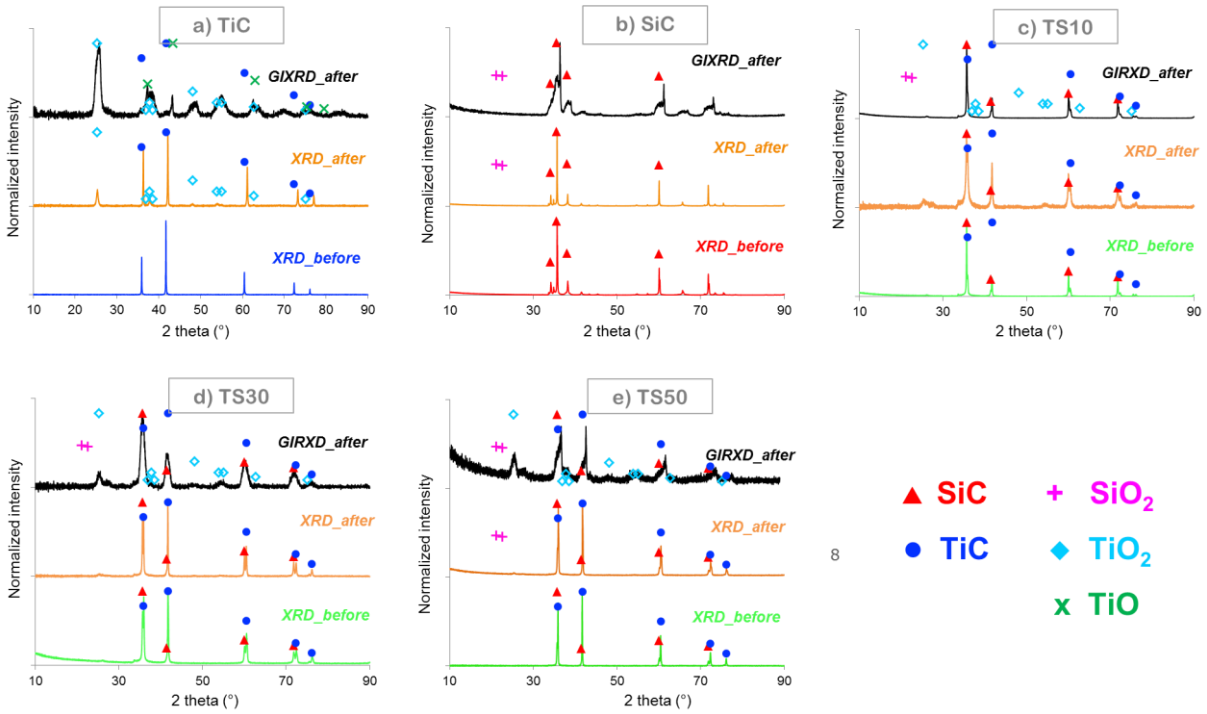

Figure 5: Grazing Incident and classical X-rays diffractograms of the samples before and after heating at 500 °C of a) pure SiC, b) pure TiC, c) TS10, d) TS30 and e) TS50. The position of SiO_2 main peaks is given as an indication to show that this phase is not detected. The comparison between the X-rays diffractograms of all samples before heating is reported in SI 2.

3.3. Oxidation resistance

In order to evaluate the oxidation resistance of the samples, thermogravimetric analyses (TGA) were performed at 1000 °C during 20 h under air on material pieces (Figure 6-a). The oxidation degree (%ox) was calculated considering the following oxidation reactions (4 and 5) [35, 47]. The mass variation due to carbon oxidation was neglected and the detailed calculation is reported in SI 4.

$$TiC + 2\,O_2 \leftrightarrow TiO_2 + CO_2 \quad (4) \qquad SiC + 2\,O_2 \leftrightarrow SiO_2 + CO_2 \quad (5)$$

After TGA analysis, the pure TiC sample is highly oxidized, up to 79 % while only 6.2 % of pure SiC is oxidized. The composites are less oxidized than the pure samples and their %ox increases with the TiC content. As pure SiC has a lower relative density than the other samples (74 % compared to > 90 %), the oxygen diffusion is favored which could induce the increase of the oxidation degree. Indeed, similar TGA measurements were conducted on TiC materials with various relative densities from a previous study [38]. The results reported in supporting information (SI 5) show that the weight gain increases when the relative density of the material decreases.

To evaluate the oxidation resistance of these samples over longer durations, sample pieces were exposed to air in a furnace at 1000 °C during 9 days. The oxidation percentage was evaluated by weighting measurements before and after oxidation (Figure 6-b). After their oxidation during 20 h in the TGA apparatus and during 9 days in a furnace, the oxidized samples were embedded in a resin and polished to study their cross-sections by SEM-EDX. The most meaningful EDX mapping are reported in Figure 7-a) and the other ones are presented in SI 6.

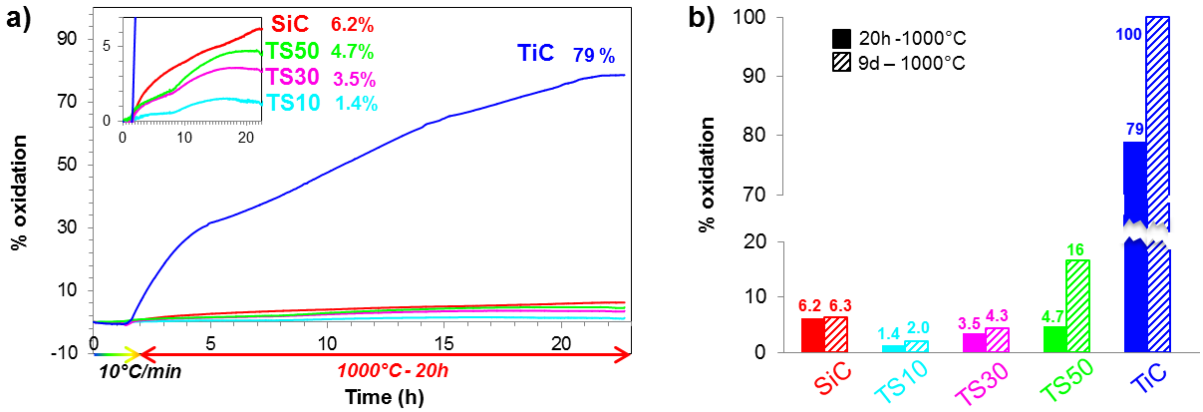

Figure 6: a) oxidation % as a function of time during TGA measurement (10 °C.min^{-1} heating up to 1000 °C followed by a 20 h dwell at 1000 °C). b) Apparent oxidation percentage after 20 h and 9 days of oxidation under air at 1000 °C. The error is about 10^{-3}% due to the precision of the weighting measurements.

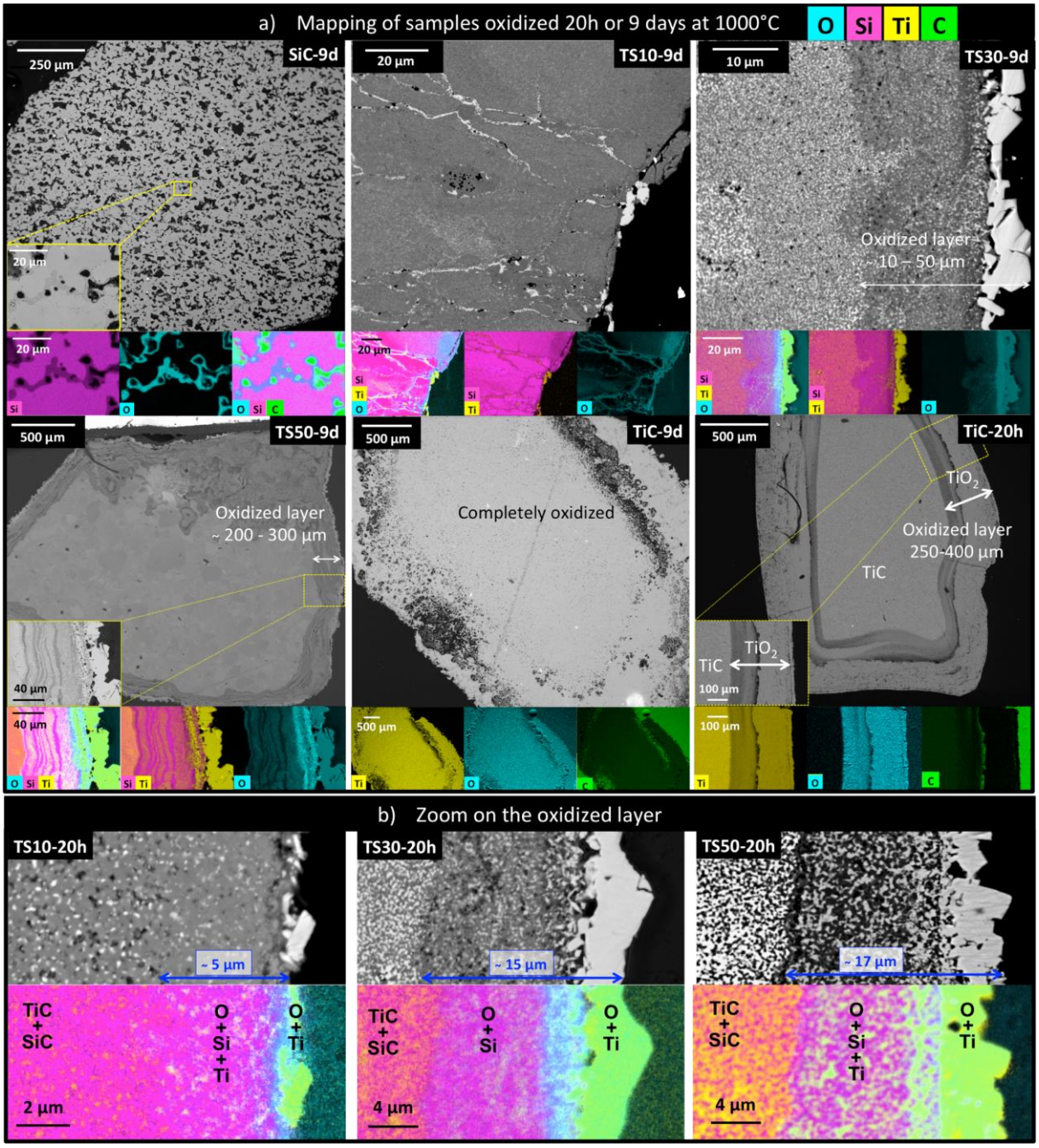

Figure 7: SEM-EDX mapping of polished cross sections of a) all samples after 9 days at 1000 °C, and pure TiC after 20h at 1000 °C. b) Zoom on the oxidized layer formed on TS10, TS30, and TS50 after 20h at 1000 °C.

After 20h or 9 days at 1000 °C, the pure SiC sample presents oxidized areas covering the pore walls, even up into the center of the material (Figure 7-a). The thickness of this oxidized layer and the ox% are similar after 20 h and 9 days (Figure 6-b), which implies that the oxidation layer is protective. After 20 h at 1000 °C, the pure TiC sample presents an oxidized layer with a thickness of about 250-400 µm, surrounding the TiC pristine core. This layer is divided into

two sublayers, the outer tends to peel as evidenced by a C enrichment at the interface due to the resin penetration. The inner layer is continuous but not protective since after 9 days at 1000 °C, the sample is completely oxidized (Figure 6-b and Figure 7-a).

In the case of TS50 sample, after 20h the oxidation layer is continuous and much thinner than that of the pure TiC (about 17 µm) (Figure 7-b and SI 6). After 9 days of oxidation, the layer has grown to reach an average thickness of 200-300 µm, it presents several demarcations oriented parallel to the surface. These demarcations are formed by areas depleted in Ti and O, mainly composed by Si and C (SI 6). The apparent ox% is three times higher after 9 days than after 20h. In the case of the TS30 sample, the oxidation layers are continuous and have close thickness after 20 h or 9 days at 1000 °C (10-20 µm). The ox% has not evolved from 20 h to 9 days at 1000 °C.

The oxidation layer of TS10 sample is not continuous, some Ti-O containing aggregates are present on the surface, and on the domain boundaries. These domains illustrate changes in composition (Ti/Si proportion) and/or porosity in the direction of the sample thickness, similarly to those observed in the direction of the sample diameter, and reported in Figure 2. Depending on their composition and porosity, these domains can form oxidized pockets. After 9 days of oxidation, the apparent ox% has increased from 1.4 to 2 %. The oxidation layer after 20 h is about 5 µm thick.

For all nanocomposites, EDX mapping at high magnification are reported in Figure 7-b. The oxidized layer can be divided into several sublayers with changes in composition. The outer sub-layer is composed of Ti and O, without Si. The inner sub-layer is partly depleted in Ti, and enriched in Si and O. As Underneath this oxidized layer, pristine SiC-TiC appears to be undamaged.

4. Discussion

4.1. Effects of the TiC proportion on the optical properties

The expected TiC-SiC overall proportions have been confirmed by SEM-EDX and XRF. SEM observations confirmed that the TiC grains have the same size in all samples but they tend to form aggregates when increasing the TiC content (Figure 2).

Before heating, the spectral reflectance at room temperature increases with the increase in the TiC proportion in the entire range of analyzed wavelengths (Figure 3 and SI 3). From the spectral reflectance curves measured at various incident angles, the total solar absorptance (α) and the hemispherical thermal emittance (ε_H) were calculated using equations (1), (2) and (3).

The results are reported as a function of the TiC content in Figure 8-a. It appears that the increase in the TiC content induces a decrease in both the absorptance (α) and the hemispherical emittance (ε_H), leading to a great increase in the spectral selectivity (α/ε_H), as observed previously for TiC-SiC composites [38]. This increase is stronger between 30 % and 50 % of TiC than in the rest of the composition ranges.

During heating, the near-normal spectral IR reflectance has been measured at various temperatures (Figure 3) leading to the calculation of the total directional thermal emittance ($\varepsilon_{8°}$), as reported in Figure 8-d). In all cases, the directional emittance increases with the heating temperature and the effect is higher when the TiC proportion increases. The increase in emittance with the measured temperature has already been reported for other borides and carbides [20, 48].

After heating and cooling, the increase in emittance is not conserved for the pure SiC sample since the hemispherical emitance values measured at room temperature before and after heating are the same (Figure 8-b). However, in the presence of TiC (pure TiC and composites), there is a difference between the absorptance and emittance values measured at room temperature before, and after heating (Figure 8-c).

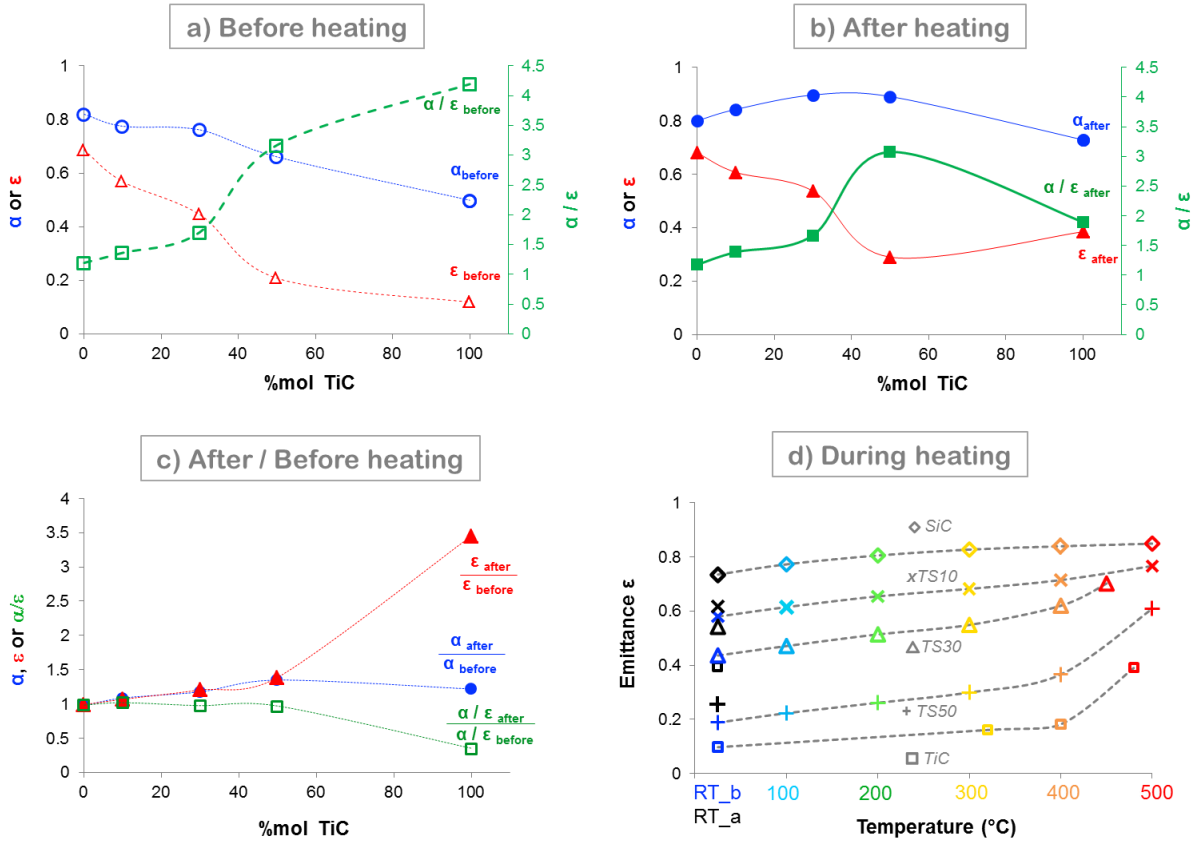

Figure 8: Absorptance (α), hemispherical emittance (ε_H) and selectivity (α/ε_H) calculated from room temperature measurements a) before heating, b) after heating and c) the ratio between them, as a function of the TiC proportion (%mol); d) directional emittance ($\varepsilon_{8°}$) as a function of the temperature of measurement.

The hemispherical emittance after heating is a little higher than before heating for all the nanocomposites and much higher for the pure TiC sample. After heating, the hemispherical emittance is even higher for the pure TiC sample than for the TS50 nanocomposite (Figure 8-b). For all samples except the pure SiC, the absorptance calculated from room temperature measurements has increased after heating (Figure 8-c). The evolution of the absorptance after heating as a function of the TiC content shows a bell shaped curve with a maximum for TS50 nanocomposite. As both the absorptance and the hemispherical emittance increase after heating, the selectivity does not change for all samples, except the pure TiC. For the latter, the increase in hemispherical emittance is too high to be compensated by the increase in absorptance, thus the selectivity decreases. These changes on the optical properties can be linked to the surface modifications observed by SEM (Figure 4). The TiC grains at the surface are oxidized, and the presence of TiO_2 and TiO is detected by XRD and GIXRD (Figure 5). An increase in the surface roughness is also reported, which could be linked to the volume gain due to the oxidation of TiC into TiO_2, and to swelling due to carbon release. Previous work showed that the increase in surface roughness induces an increase in both the absorptance and the emittance [38].

4.2. Effects of the SiC content on the oxidation resistance

The low relative density and high open porosity of pure SiC sample favored O penetration and produced an oxidized layer on the pore walls, even up into the center of the sample. This correlation between low relative density and high oxidation degree is confirmed by TGA oxidation procedure applied to several TiC materials with various relative densities (SI 5). However, the thickness of the oxidized layer and the %ox calculated from weight gain did not increase between 20 h and 9 days. Therefore, the oxidation layer appears to be protective. According to the litterature, this layer could be SiO_2, as it was reported during the passive oxidation of SiC at temperatures below 1400 °C [47, 49, 50]. For temperatures above 1400 °C, SiC endures active oxidation releasing gaseous SiO.

Pure TiC sample is completely oxidized after 9 days at 1000 °C. The oxidation of TiC into TiO_2 and TiO has already been widely reported in the literature [35, 39, 51-53]. Depending on the

particle size, the temperature of oxidation of TiC can vary, nevertheless it starts around 380 °C, and follows four stages [52]. First TiC is oxidized into oxycarbide $TiC_xO_{(1-x)}$, then it forms suboxides (TiO, Ti_3O_5 or Ti_4O_9), followed by the formation of anatase (TiO_2), and finally it evolves toward rutile (TiO_2). The oxidation layer is usually divided into two sub-layers; TiO_2 on top of sub-oxides like Ti_3O_5, Ti_4O_7. These two sub-layers are present on the pure TiC sample oxidized after 20 h but not after 9 days. The oxidation kinetics of TiC depend on the diffusion of O through the material, which explains the substoichiometry of the inner layer and the higher oxidation degree for less dense samples [35, 54, 55]. After 9 days of oxidation, O has diffused enough through the material to produce a single layer of TiO_2.

In the case of the composites, the oxidation layer can be divided into two sub-layers. Ti is concentrated at the surface, forming TiO_2 aggregates for the lowest Ti composition (TS10) and a continuous layer of TiO_2 for richer ones (TS30 and TS50). Underneath, the inner layer is highly depleted in Ti, which means that Ti has diffused somehow toward the surface during the oxidation. The inner Si, O rich layer could be SiO_2. This layer appears to form a continuous and protective barrier for samples with enough Si (TS10 and TS30) but not for the composition with lower Si content (TS50). These results are consistent with the oxidation study of TiC/SiC composites by Banu et al. [39]. They observed embedded TiC particles in a SiC matrix, with the presence of SiO_2 and TiO_2 after the oxidation at 750 °C under static air. Furthermore, Baux *et al.* synthesized porous TiC-SiC ceramics by Chemical Vapor Infiltration (CVI) of SiC into cellular TiC structures [56]. After 10 hours of oxidation at 1000 °C, TiC was oxidized into TiO_2 and suboxides in the core of the sample, whereas TiC parts located near the surface were protected from oxidation by a layer of SiC. They concluded that this difference was due to the inhomogenous penetration of SiC deposed by CVI. However, they did not report the oxidation of SiC into SiO_2 nor the presence of any Ti-depleted layer underneath. To our knowledge, the formation at 1000 °C of a SiO_2 layer underneath a TiO_2 crust has not been reported in the literature. Therefore, ongoing work is conducted to study in more detail the processes involved in the formation of these sub-layers during TiC-SiC composite oxidation.

4.3. Comparision with other materials

The literature reports several studies concerning the optical properties of UHTCs and especially of borides and carbides. Our pure TiC sample, with a spectral selectivity of 5.0, approaches the best one reported so far: dense LaB_2 ($\alpha/\varepsilon = 6.4$ [57]). The spectral selectivity of TS30 and TS50 composites (1.7 and 3.2) are superior to pure SiC (1-1.1 [58] and this study). They are in the same range as $MoSi_2$ added carbides (2.2 for HfC, 2.4 for ZrC, and 2.8 for TaC [59]), pure

borides (2.5 for HfB_2, 3.9 for ZrB_2 and 4.0 for TaB_2 [22, 58], 2.2 for TiB_2 [60]), and composites (2.2 for HfB_2-SiC and 2.8 for HfB_2-HfC-SiC [61]). This comparison is given as an indication since the spectral selectivity values originate from emittance measurements at different temperatures. Indeed, it has been reported that the emittance measured at room temparature is usually underestimated compared to the one measured at higher temperatures [12], thereby impacting the spectral selectivity. However, in all cases, the samples did not experienced oxidation since measurements were conducted at room temperature or at high temperature measurements under vaccum or inert atmosphere.

The optical properties of UHTCs after exposition to oxidation are little studied so far. TaB_2 sumitted to helium or air atmosphere during 20 min at 827 °C loses completely its spectral selectivity [62], the spectral selectivity of ZrB_2 + 10% $MoSi_2$ decreases toward 1, and reaches the one of pure SiC after heating up to 1200 °C [63]. The results obtained for HfB_2-SiC composite are better since the spectral selectivity after oxidation at 927°C during 5h is still of 1.3 (compared to 2.2 before oxidation) and the addition of HfC in this HfB_2-SiC composite did not improve the results ($\alpha/\varepsilon = 0.6$ after oxidation), probably because the amount of SiC was too low [61]. In this context, our TiC-SiC composites are quite performant since TS30 and TS50 samples have a spectral selectivity of 1.7 and 3.1 after oxidation at 500°C. Even though these values were obtained at lower temperatures, the oxidation tests at 1000 °C revealed the formation of a protective SiO_2 layer which suggests that the TiC-SiC composites could keep their interesting spectral selectivity at high temperatures.

Conclusion

This study assessed both the optical properties and the oxidation resistance of SiC-TiC nanocomposite densified materials while heating up to 500 °C. The effects of the TiC proportion (10 to 50 %at) were studied and compared to pure TiC and SiC samples. The spectral selectivity was found to increase with the TiC content due to a high decrease in emittance and despite a low decrease in absorptance. The samples were heated up to 500 °C to measure the reflectance in the 1.25 to 25 µm wavelength range, and determine their optical properties at various temperatures. The emittance increases with the heating temperature. After heating, the pure SiC sample remains unoxidized, whitout any changes in its optical properties, while pure TiC sample experiences severe oxidation and high decrease in its spectral selectivity. The composites are also partly oxidized, and more severly as the TiC content increased. The oxidation of TiC grains TiO_2, leads to an increase in the surface roughness which induces an

increase in both the emittance and the absorptance. Contrary to the pure TiC sample, for the composites, the increase in emittance is compensated by the increase in the absorptance. Therefore, the selectivity of the composites remains the same after exposure to air at 500 °C. Oxidation tests at 1000 °C during 20 h and 9 days confirmed the dramatic TiC sensitivity to oxidation and the good oxidation resistance of SiC. The TiC-SiC composites form an oxidized layer mainly composed of a TiO_2 outer sub-layer and a SiO_2 inner sub-layer. The latter appears to be protective when the Si content is high enough (70 at% at least). According to all these results, the 30 % TiC – 70 % SiC composite seems to display both high spectral selectivity and satisfactory oxidation resistance, which are required properties for solar absorber applications.

Conflicts of interest

There are no conflicts to declare.

Acknowledgments

This work was funded by the National Agency for Research (ANR) of the French State, in the framework of the CARAPASS project (award n°ANR-16-CE08-0026) and of the French "Investments for the future" program managed by ANR under contracts ANR-10-LABX-22-01-SOLSTICE and ANR-10-EQPX-49-SOCRATE. We wish to thank Renaud Podor and Joseph Lautru for SEM imaging, Bruno Corso for XRD assistance, Cyrielle Rey for furnace assistance, Jeremy Causse for XRF measurements, and Christophe Escape and Jose Maria Osorio for their help in reflectometry measurements.

References

1. Granqvist, C.G., *Solar energy materials.* Advanced Materials, 2003. **15**(21): p. 1789-1803.
2. Tian, Y. and C.Y. Zhao, *A review of solar collectors and thermal energy storage in solar thermal applications.* Applied Energy, 2013. **104**: p. 538-553.
3. Spitz, J., *Selective surfaces for high-temperature solar photothermal conversion.* Thin Solid Films, 1977. **45**(1): p. 31-41.
4. Spitz, J. and D. Mazierebezes, *Selective materials for solar-energy photothermal conversion.* Journal of Optics-Nouvelle Revue D Optique, 1984. **15**(5): p. 325-332.
5. Bogaerts, W.F. and C.M. Lampert, *Materials for photothermal solar-energy conversion.* Journal of Materials Science, 1983. **18**(10): p. 2847-2875.
6. Lampert, C.M., *Coatings for enhanced photo thermal energy collection .1. Selective absorbers.* Solar Energy Materials, 1979. **1**(5-6): p. 319-341.
7. Agrafiotis, C.C., et al., *Evaluation of porous silicon carbide monolithic honeycombs as volumetric receivers/collectors of concentrated solar radiation.* Solar Energy Materials and Solar Cells, 2007. **91**(6): p. 474-488.

8. Burlafinger, K., A. Vetter, and C.J. Brabec, *Maximizing concentrated solar power (CSP) plant overall efficiencies by using spectral selective absorbers at optimal operation temperatures.* Solar Energy, 2015. **120**: p. 428-438.
9. Sani, E., et al., *Ultra-High Temperature Ceramics for solar receivers: spectral and high-temperature emittance characterization.* Journal of the European Optical Society-Rapid Publications, 2012. **7**.
10. Blau, H.H. and J.R. Jasperse, *Spectral emittance of refractory materials.* Applied Optics, 1964. **3**(2): p. 281-&.
11. Mercatelli, L., M. Meucci, and E. Sani, *Design and test of a new facility for assessing spectral normal emittance of solid materials at high temperature*, in *Optical Components and Materials Xiii*, S. Jiang and M.J.F. Digonnet, Editors. 2016.
12. Mercatelli, L., M. Meucci, and E. Sani, *Facility for assessing spectral normal emittance of solid materials at high temperature.* Applied Optics, 2015. **54**(29): p. 8700-8705.
13. Sani, E., et al., *Optical properties of black and white ZrO2 for solar receiver applications.* Solar Energy Materials and Solar Cells, 2015. **140**: p. 477-482.
14. Sani, E., et al., *Optical properties of boride ultrahigh-temperature ceramics for solar thermal absorbers.* Journal of Photonics for Energy, 2014. **4**.
15. Sciti, D., et al., *Tantalum diboride-based ceramics for bulk solar absorbers.* Solar Energy Materials and Solar Cells, 2014. **130**: p. 208-216.
16. Sani, E., et al., *Porous and dense hafnium and zirconium ultra-high temperature ceramics for solar receivers.* Optical Materials, 2013. **36**(2): p. 163-168.
17. Sciti, D., et al., *Suitability of ultra-refractory diboride ceramics as absorbers for solar energy applications.* Solar Energy Materials and Solar Cells, 2013. **109**: p. 8-16.
18. Sani, E., et al., *Hafnium and tantalum carbides for high temperature solar receivers.* Journal of Renewable and Sustainable Energy, 2011. **3**(6).
19. Sani, E., et al., *Ultra-refractory ceramics for high-temperature solar absorbers.* Scripta Materialia, 2011. **65**(9): p. 775-778.
20. Mercatelli, L., et al., *Ultra-refractory diboride ceramics for solar plant receivers.* Proceedings of the Solarpaces 2013 International Conference, 2014. **49**: p. 468-477.
21. Sani, E., et al., *Compositional dependence of optical properties of zirconium, hafnium and tantalum carbides for solar absorber applications* Solar Energy, 2016. **- 131**(-): p. - 207.
22. Sani, E., et al., *Optical properties of dense zirconium and tantalum diborides for solar thermal absorbers.* Renewable Energy, 2016. **91**: p. 340-346.
23. Sani, E., et al., *Optical properties of ZrB2 porous architectures.* Solar Energy Materials and Solar Cells, 2016. **144**: p. 608-615.
24. Sani, E., et al., *Process and composition dependence of optical properties of zirconium, hafnium and tantalum borides for solar receiver applications.* Solar Energy Materials and Solar Cells, 2016. **155**: p. 368-377.
25. Antou, G., et al., *Thermomechanical properties of a spark plasma sintered ZrC-SiC composite obtained by a precursor derived ceramic route.* Materials Science and Engineering a-Structural Materials Properties Microstructure and Processing, 2015. **643**: p. 1-11.
26. Fahrenholtz, W.G., et al., *Refractory diborides of zirconium and hafnium.* Journal of the American Ceramic Society, 2007. **90**(5): p. 1347-1364.
27. Wuchina, E., et al., *Designing for ultrahigh-temperature applications: The mechanical and thermal properties of HfB2, HfCx, HfNx, and alpha Hf(N).* Journal of Materials Science, 2004. **39**(19): p. 5939-5949.
28. Mroz, C., *Zirconium diboride.* American Ceramic Society Bulletin, 1994. **73**(6): p. 141-142.

29. Coulibaly, M., et al., *From colloidal precursors to metal carbides nanocomposites MC (M=Ti, Zr, Hf and Si): Synthesis, characterization and optical spectral selectivity studies.* Solar Energy Materials and Solar Cells, 2015. **143**: p. 473-479.
30. Charpentier, L., et al., *High temperature oxidation of Zr- and Hf-carbides: Influence of matrix and sintering additive.* Journal of the European Ceramic Society, 2013. **33**(15-16): p. 2867-2878.
31. Charpentier, L., et al., *Microstructural characterization of ZrC-MoSi2 composites oxidized in air at high temperatures.* Applied Surface Science, 2013. **283**: p. 751-758.
32. Onuma, A., et al., *High temperature oxidation of sintered TiC in an H2O-containing atmosphere.* Solid State Ionics, 2004. **172**(1-4): p. 417-419.
33. Shimada, S., *A thermoanalytical study on the oxidation of ZrC and HfC powders with formation of carbon.* Solid State Ionics, 2002. **149**(3-4): p. 319-326.
34. Shimada, S. and K. Mochidsuki, *The oxidation of TiC in dry oxygen, wet oxygen, and water vapor.* Journal of Materials Science, 2004. **39**(2): p. 581-586.
35. Gherrab, M., et al., *Oxidation behavior of nano-scaled and micron-scaled TiC powders under air.* International Journal of Refractory Metals & Hard Materials, 2013. **41**: p. 590-596.
36. Sempere, J., et al., *Thermal behavior of oxidation of TiN and TiC nanoparticles.* Journal of Thermal Analysis and Calorimetry, 2011. **105**(2): p. 719-726.
37. Rudneva, V.V. and G.V. Galevskii, *Investigation of thermal oxidation resistance of nanopowders of refractory carbides and borides.* Russian Journal of Non-Ferrous Metals, 2007. **48**(2): p. 143-147.
38. Aréna, H., et al., *SiC-TiC nanocomposite for bulk solar absorbers applications: Effect of density and surface roughness on the optical properties.* Solar Energy Materials and Solar Cells, 2019. **191**: p. 199-208.
39. Banu, N.D., et al., *Identification of selective oxidation of TiC/SiC composite with X-ray diffraction and Raman spectroscopy.* Chemical Papers, 2016. **70**(11): p. 1503-1511.
40. Pizon, D., et al., *Oxidation behavior of spark plasma sintered ZrC-SiC composites obtained from the polymer-derived ceramics route.* Ceramics International, 2014. **40**(3): p. 5025-5031.
41. Tripp, W.C., H.H. Davis, and H.C. Graham, *Effect of an SiC addition on oxidation of ZrB2.* American Ceramic Society Bulletin, 1973. **52**(8): p. 612-616.
42. Deschanels, X., et al., *Comparison of two soft chemistry routes for the synthesis of mesoporous carbon/beta-SiC nanocomposites.* Journal of Materials Science, 2013. **48**(11): p. 4097-4108.
43. Diago, M., et al., *Characterization of desert sand to be used as a high-temperature thermal energy storage medium in particle solar receiver technology.* Applied Energy, 2018. **216**: p. 402 - 413.
44. Soum-Glaude, A., et al., *Optical characterization of TiAlNx/TiAlNy/Al2O3 tandem solar selective absorber coatings.* Solar Energy Materials and Solar Cells, 2017. **170**: p. 254 - 262.
45. Khalil, N.Z., et al., *Effect of Particle Size Distribution on SiC Ceramic Sinterability.* Materials Transactions, 2015. **56**(11): p. 1827-1833.
46. Lara, A., et al., *Densification of additive-free polycrystalline beta-SiC by spark-plasma sintering.* Ceramics International, 2012. **38**(1): p. 45-53.
47. Ramberg, C.E., et al., *Passive-oxidation kinetics of high-purity silicon carbide from 800 degrees to 1100 degrees C.* Journal of the American Ceramic Society, 1996. **79**(11): p. 2897-2911.
48. Sani, E., et al., *Porous and dense hafnium and zirconium ultra-high temperature ceramics for solar receivers.* Optical Materials, 2013. **36**(2): p. 163-168.

49. Liu, D.M., *Oxidation of polycrystalline alpha-silicon carbide ceramic.* Ceramics International, 1997. **23**(5): p. 425-436.
50. Costello, J.A., I.S.T. Tsong, and R.E. Tressler, *OXYGEN PENETRATION INTO SIC CERAMICS DURING THERMAL-OXIDATION.* American Ceramic Society Bulletin, 1981. **60**(3): p. 379-379.
51. Shimada, S., *A thermoanalytical study of oxidation of TiC by simultaneous TGA-DTA-MS analysis.* Journal of Materials Science, 1996. **31**(3): p. 673-677.
52. Shimada, S. and M. Kozeki, *Oxidation of TiC at low-temperatures.* Journal of Materials Science, 1992. **27**(7): p. 1869-1875.
53. Zhang, L.H. and R.V. Koka, *A study on the oxidation and carbon diffusion of TiC in alumina titanium carbide ceramics using XPS and Raman spectroscopy.* Materials Chemistry and Physics, 1998. **57**(1): p. 23-32.
54. Zainulin, Y.G., S.I. Alyamovsky, and G.P. Shveikin, *Concerning structural mechanism of oxygen inclusion into lattice of titanium carbide.* Journal of Physics and Chemistry of Solids, 1978. **39**(1): p. 29-31.
55. Schuhmacher, M. and P. Eveno, *Oxygen diffusion in titanium carbide.* Solid State Ionics, 1984. **12**(MAR): p. 263-270.
56. Baux, A., et al., *Synthesis and properties of multiscale porosity TiC-SiC ceramics.* Journal of the European Ceramic Society, 2019. **39**(8): p. 2601-2616.
57. Sani, E., et al., *Lanthanum hexaboride for solar energy applications.* Scientific Reports, 2017. **7**.
58. Sciti, D., et al., *Suitability of ultra-refractory diboride ceramics as absorbers for solar energy applications.* Solar Energy Materials and Solar Cells, 2013. **109**: p. 8-16.
59. Sani, E., et al., *Compositional dependence of optical properties of zirconium, hafnium and tantalum carbides for solar absorber applications.* Solar Energy, 2016. **131**: p. 199-207.
60. Sani, E., et al., *Titanium diboride ceramics for solar thermal absorbers.* Solar Energy Materials and Solar Cells, 2017. **169**: p. 313-319.
61. Musa, C., et al., *Optical characterization of hafnium boride and hafnium carbide-based ceramics for solar energy receivers* Solar Energy, 2018. **169**: p. 111-119.
62. Charpentier, L. and C. Caliot, *The impact of the oxidation on the optical properties of TaC.* Solar Energy Materials and Solar Cells, 2017. **171**: p. 16-23.
63. Silvestroni, L., et al., *An overview of ultra-refractory ceramics for thermodynamic solar energy generation at high temperature.* Renewable Energy, 2019. **133**: p. 1257-1267.
64. Coulibaly, M., *Carbures nanocomposites issus de précurseurs s ol-gel et impacts sur la sélectivité optique* 2015, Montpellier.

Supporting information

SI 1: Synthesis route and material characterization devices and conditions

Synthesis

The nanocomposites were prepared using a semi-molecular route involving hydrolysis and polycondensation of alkoxides as metal oxide precursors and sucrose as carbon source. The resulting powders were subjected to two heat treatments to decompose the sucrose and citric acid into carbon (800 °C Equations 1 and 2) and then for the carbothermal reduction of oxides into carbide (1550 °C Equation 3).

Sucrose and citric acid decomposition - T = 800 °C

$$\begin{cases} C_{12}H_{22}O_{11(s)} \rightarrow \mathbf{12}\ \boldsymbol{C_{(s)}} + 11\ H_2O_{(g)} & (1) \\ C_6H_8O_{7(s)} \rightarrow \mathbf{6}\boldsymbol{C_{(s)}} + 4\ H_2O_{(g)} + \frac{3}{2}\ O_{2(g)} & (2) \end{cases}$$

Carbothermal reduction - T = 1550 °C

$$MO_{2(s)} + 3\ C_{(s)} \rightarrow MC_{(s)} + 2\ CO_{(g)} \qquad (3)$$

$$R = \frac{12*n_{C_{12}H_{22}O_{11}}}{3*n_{MO_2}} + \frac{6*n_{C_6H_8O_7}}{3*n_{MO_2}} \qquad (4) \qquad F = \frac{n_{Ti}}{n_{Ti}+n_{Si}} = \frac{n_{TTIP}}{n_{TTIP}+n_{TEOS}} \qquad (5)$$

The ratio R (Equation 4) quantifies the carbon content resulting from the decomposition of sucrose and citric acid according to the Equations (1) and (2). Because the decomposition of sucrose and citric acid produces not only effective carbon but also carbon gaseous species, the amount of carbon available for the carbothermal reduction is not easily predictable and varies depending on the conditions. The value of the R ratio leading to a stoichiometric carbothermal reaction is empirical. The values of R ratio are deduced according to preliminary studies [64]. The relative proportions of Si and Ti in the final composite were controlled by the F ratio, defined by Equation 5. The amounts of TEOS and TTIP used in the synthesis were adapted to produce composites with increasing F ratios as described in Table 1. For the pure TiC and pure SiC references, commercial products supplied by Sigma Aldrich were used with a purity of 98 % and 97.5 %, respectively.

Sample	TS10	TS30	TS50	TiC	SiC
R	1.68	2.39	3.18	Commercial products	
F (%at)	10	30	50	100	0
F* (%wt)	14,3	39	60	100	0
$T_{sintering}$ (°C)	1750			1700	1950

Table 3: Name, R and F ratios and sintering temperature for each sample used in this study.

Porosity, density and roughness

Archimedes method was used to measure the apparent density ($\rho_{app.}$) of the sample by hydrostatic weighing in water at 21 °C. The pycnometric density ($\rho_{pycno.}$) of each sample was determined by helium pycnometry. The theoretical density ($\rho_{th.}$) was calculated based on the average Ti / Si proportion measured by SEM-EDX and XRF analyses, and the C and O content measured by elemental analyses. The relative density (D), the open and closed porosity (ϕ_{open} and ϕ_{closed}) were estimated according to Equations 6, 7 and 8, respectively.

$$D = \frac{\rho_{app.}}{\rho_{th.}} \quad (6) \qquad \phi_{open} = 1 - \frac{\rho_{app.}}{\rho_{pycno.}} \quad (7) \qquad \phi_{closed} = \frac{\rho_{app.}}{\rho_{pycno.}} - \frac{\rho_{app.}}{\rho_{th.}} \quad (8)$$

Optical interferometry was used to measure the surface roughness Ra of the samples (Fogal Nanotech – Microsurf 3D). For each sample, at least six areas of 287 µm x 481 µm, were analyzed to obtain an average roughness value.

Morphology and composition

The morphology of the samples was studied by Scanning Electron Microscopy (SEM), with an FEI Quanta 200 ESEM equipped with a Field Emission Gun, and with a Tescan VEGA3 equipped with a W thermo-cationic gun. Energy Dispersive Spectra (EDX) were recorded using a Bruker SDD 5030 detector with a 123 eV resolution at the Mn (Kα) line. EDX was used to confirm the composition of the synthesized products and to study the effects of oxidation.
The global Ti/Si proportion was also analyzed by X-Ray Fluorescence (XRF), using a Spectro-Xepos apparatus with four secondary targets (Mo, Al_2O_3, Co and HOPG Bragg crystal).

Carbon and Oxygen analyzers (LECO CS230 and TCH600) were used to measure the total carbon and oxygen contents, respectively. The samples were heated under oxygen for carbon analysis, or with graphite addition under helium gas for oxygen analysis. In both cases, the formation of carbon oxides was detected and quantified by infrared spectroscopy, then related to the total carbon or oxygen content in the samples. Added Fe powder was used to assist the combustion in the case of carbon analysis.
Thermogravimetric analyses (Setsys - 1750 CS Evol, Setaram) were conducted to evaluate the oxidation resistance of the samples. Sample pieces weighting about 20 mg were subjected to a 20 h dwell at 1000 °C. The heating rates of rise and cooling were 10 °C.min^{-1} and 30 °C.min^{-1}, respectively.

Structure

The samples were characterized by X-Ray Diffraction (XRD) using the Bruker D8 advance diffractometer equipped with lynxeye detector and using Cu Kα radiation (λ=1.54184Å). Data were acquired in reflection geometry (parallel beam) in the 10-90° (2θ mode) range of angles with steps of 0.019°. Silicon powder was collected and used as standard to evaluate the instrumental function. TiC compound crystallized in the cubic NaCl structure type in the Fm-3m space group, whereas SiC crystallized in the ZnS structure type in the F-43m space group. Grazing Incident X-Ray Diffraction (GI-XRD) measurements were performed using a Bruker D8 Advance diffractometer and primary optics adopting the Bragg − Brentano geometry. Secondary optics were composed of long Sollers slits of 0.12° and of a point detector. GI-XRD patterns were collected between 10° and 90° (2θ mode) with a 0.02° step. The angular domain was limited at higher angles by the beam knife-edge that equipped the reflectivity stage. The incident angle, θi, was fixed to a value of 0.4°.

Optical properties

Two spectrophotometers were used to measure the total spectral reflectance of the samples. Over the wavelength range from 0.25 to 2 µm, the near-normal hemispherical ($R^{\perp,\cap}$) reflection spectrum was acquired with a 10 nm step using a Perkin Elmer Lambda 950 spectrophotometer. This apparatus was equipped with deuterium and tungsten lamps, PMT and InGaAs detectors, and a 150 mm integrating sphere coated with Spectralon diffuse reflective coating. The sample was illuminated at an incidence angle of 8°.

Over the wavelength range from 1.25 µm to 25 µm, the hemispherical directional reflectance ($R^{\cap,\theta}$) was recorded at different detection angles θ from 8 to 80°, using a SOC-100 HDR reflectometer (Surface Optics Corporation) coupled with a Nicolet FTIR 6700 spectrophotometer. A gold coated calibrated specular reflectance standard was used as reference during measurements (NIST calibration). The spectral range from 1.25 to 25 µm was covered by a FTIR equipped with InGaAs and DTGS/KBr detectors, coupled with Quartz and KBr beamsplitters, respectively. The sample was illuminated from all directions using a 700 °C (973 K) blackbody as the infrared source and a 2π imaging gold coated hemiellipsoid. The light reflected by the sample at a chosen detection angle was collected by a moveable overhead mirror which directed the collimated beam into the FTIR apparatus for signal treatment to retrieve the reflectance spectrum. Each reflectance spectrum was derived from 64 consecutive scans on the same sample. A heating plate on the sample holder enabled measurements at

different temperatures (from room temperature to 500 °C). The temperature of the sample was controlled by a surface thermocouple connected to PID regulation of the heating resistance. The complete description of the devices used is detailed in [43, 44].

The total spectral reflectance measured and the solar spectrum were interpolated over the wavelength range from 0.25 to 25 µm with a step of 2 nm to calculate the optical parameters, using Mathematica software. The solar absorptance α was calculated from room temperature measurements in the wavelength range 0.25 to 4 µm according to Equation 9. The near-normal thermal emittance $\varepsilon_{8°}(T)$ and the hemispherical emittance $\varepsilon_H(T_a)$ at room temperature were calculated in the wavelength range from 1.25 to 25 µm according to Equations 10 and 11 respectively. The hemispherical emittance represents the propensity of a surface illuminated from all directions of the hemisphere surrounding it to reemit radiation in the same hemisphere. Spectral transmittance was not measured, as the samples were opaque over the whole considered spectral range.

$$\alpha = \frac{\int_{0.25\ \mu m}^{4\ \mu m}[1-R_{8°}(\lambda, T_a)]\cdot G(\lambda)\cdot d\lambda}{\int_{0.25\ \mu m}^{4\ \mu m} G(\lambda)\cdot d\lambda} \qquad (9)$$

$$\varepsilon_\theta(\theta, T) = \frac{\int_{1.25\ \mu m}^{25\ \mu m}[1-R(\lambda, T, \theta)]\cdot P(\lambda, T)\cdot d\lambda}{\int_{1.25\ \mu m}^{25\ \mu m} P(\lambda, T)\cdot d\lambda} \qquad (10)$$

$$\varepsilon_H(T_a) = 2\int_0^{\pi/2} \varepsilon_\theta(\theta, T_a)\cdot \sin\theta \cdot \cos\theta \cdot d\theta \qquad (11)$$

λ is the wavelength [µm]. $R_{8°}(\lambda,T)$ and $R(\lambda,T_a,\theta)$ are the spectral reflectance of the sample measured at various temperatures (T) and a detection angle of 8°, or at room temperature (T_a) with a variable detection angle θ. $G(\lambda)$ is the standard solar irradiance spectrum (ASTM-G173 AM1.5 direct + circumsolar) [W.m^{-2}.µm]. $P(\lambda,T)$ is the spectral emittance (exitance) of a blackbody at temperature T derived from Planck's law [W.m^{-2}.µm].

SI 2: X-ray diffractograms before heating

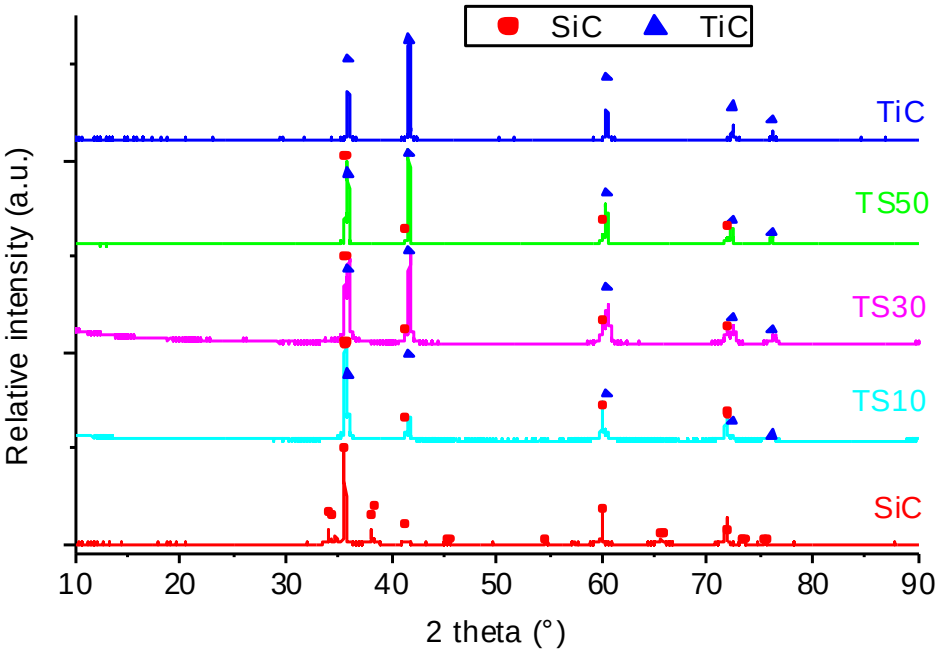

Figure 9: a) XRD diffractograms for all samples measured at room temperature before heating.

SI 3: Reflectance curves

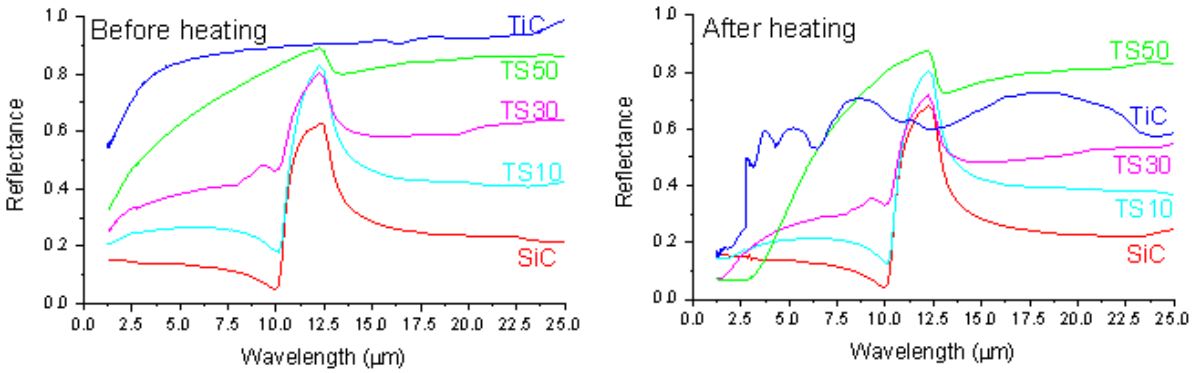

Figure 10: Total near normal spectral reflectance for all samples measured with an incident angle of 8°, at room temperature before heating (left column) and after heating (right column).

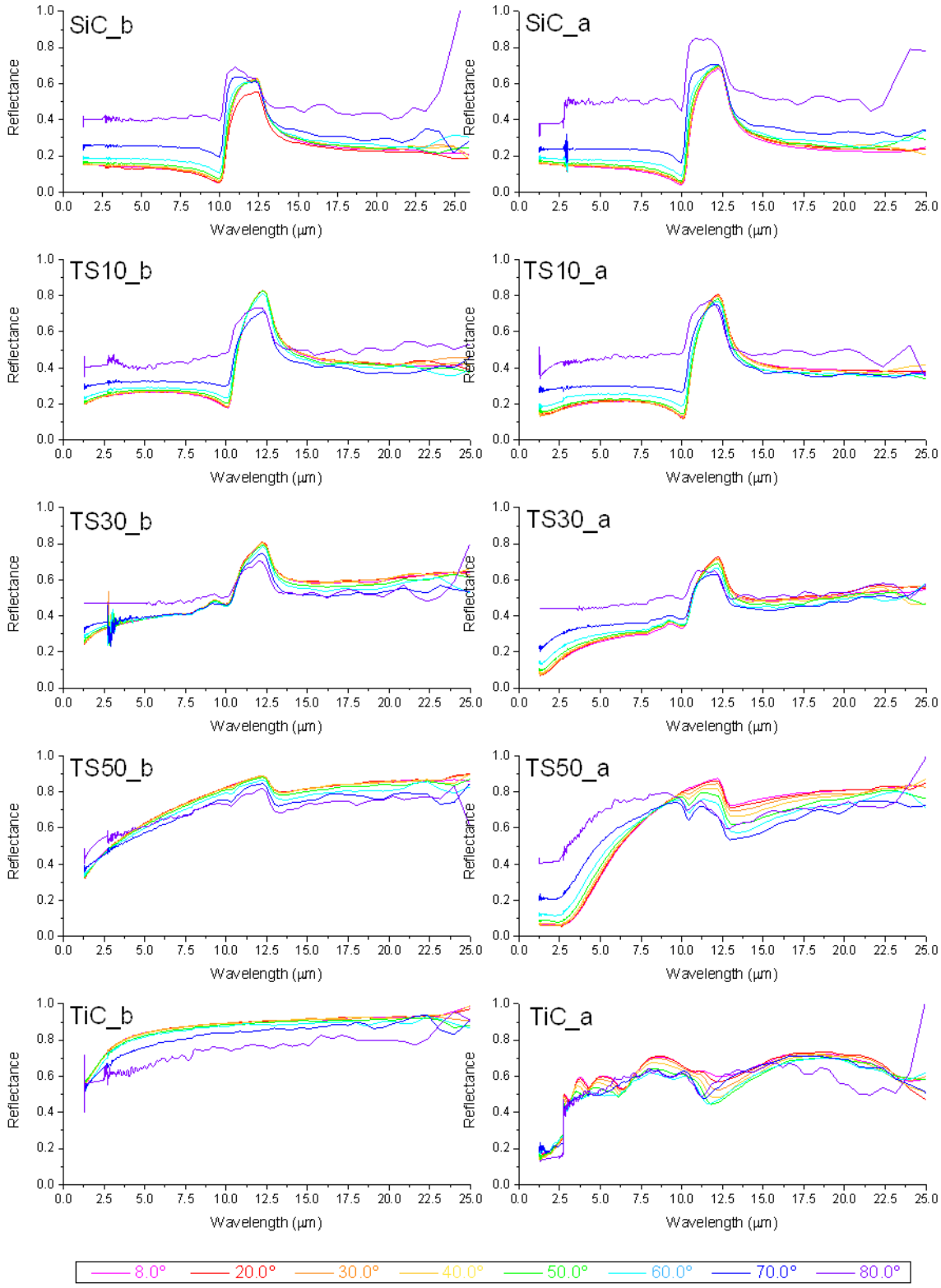

Figure 11: Total near normal spectral reflectance for all samples measured with various detection angles at room temperature before heating (left column) and after heating (right column).

SI 4: Oxidation percentage calculation

From the TGA results, the relative mass gain $(\Delta m/m)_{exp}$ was calculated. According to the TiC and SiC oxidation reactions 12 and 13, if TiC and SiC are completely oxidized into TiO_2 and SiO_2, the maximum relative mass gain $(\Delta m/m)_{max}$ would be described by Equation 14. In this calculation, the mass variation due to carbon oxidation is neglected.

$$TiC + 2O_2 \leftrightarrow TiO_2 + CO_2 \quad (12) \qquad SiC + 2\,O_2 \leftrightarrow SiO_2 + CO_2 \quad (13)$$

$$\left(\frac{\Delta m}{m}\right)_{max} = \frac{M_{oxides}}{M_{carbides}} - 1 = \frac{F \times M_{TiO_2} + (1-F) \times M_{SiO_2}}{F \times M_{TiC} + (1-F) \times M_{SiC}} - 1 \quad (14)$$

with F the TiC molar fraction (%mol) and M the molar mass ($g.mol^{-1}$). The maximum relative mass gain is 50 % for pure SiC, 47.6 % for TS10, 43.5 % for TS30, 40.0 % for TS50 and 33.3 % for pure TiC. The oxidation percentage (%ox) is the ratio between the experimental relative mass gain and the maximum relative mass gain, as described by Equation 15:

$$\%ox = \frac{\left(\frac{\Delta m}{m}\right)_{exp}}{\left(\frac{\Delta m}{m}\right)_{max}} \times 100 \quad (15)$$

SI 5: TG analyses of TiC samples with various densities

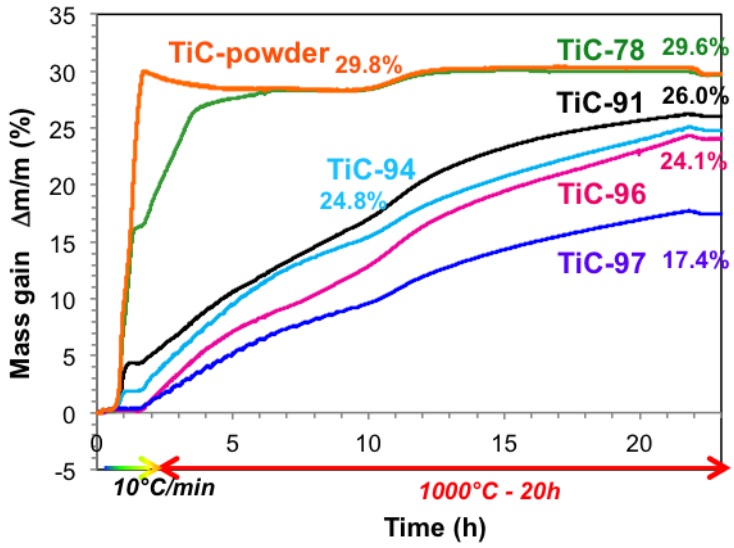

Figure 12: Evolution of the weight gain as a function of time during TGA measurement (10 °C.min^{-1} rise up to 1000 °C followed by a 20 h dwell at 1000 °C) for TiC samples with a relative density of 97 %, 96 %, 94 %, 91 %, 78 % and powder.

SI 6: EDX-mapping after 20 h or 9 days of oxidation at 1000°C under air.

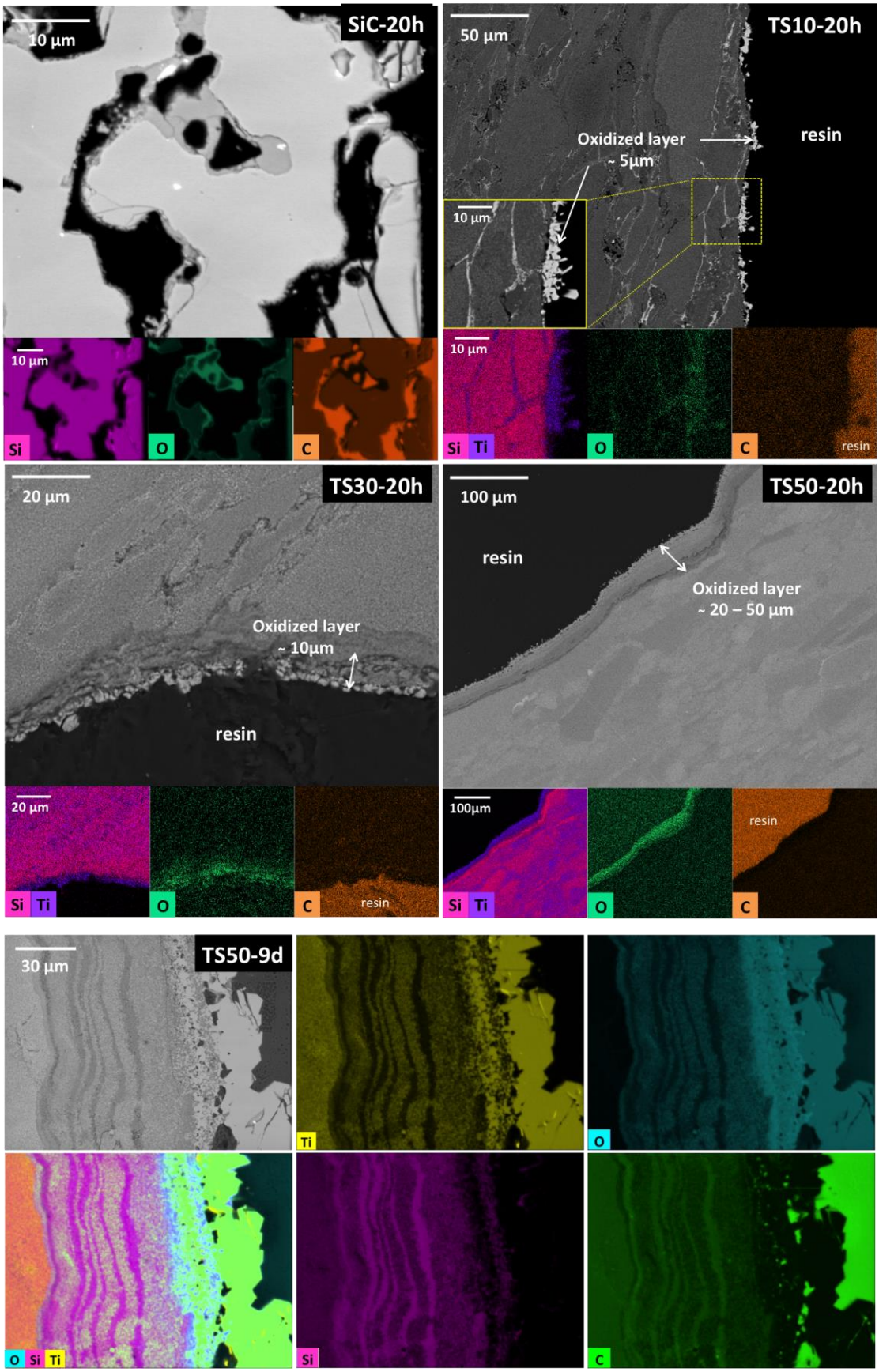

Figure 13: SEM-EDX mapping of the samples oxidized 20 h or 9 days at 1000°C under air.